Oxid Met (2018) 89:483–498
https://doi.org/10.1007/s11085-017-9801-x

ORIGINAL PAPER

# Effect of Pressure on Metal Dusting Initiation on Alloy 800H and Alloy 600 in CO-rich Syngas

**S. Madloch**[1] · **A. S. Dorcheh**[1] · **M. C. Galetz**[1]

Received: 3 May 2017 / Revised: 16 August 2017 / Published online: 1 September 2017


**Abstract** The effect of pressure on metal dusting initiation was studied by exposing conventional alloys 600 and 800H in CO-rich syngas atmosphere ($H_2$, CO, $CO_2$, $CH_4$, $H_2O$) at ambient and 18 bar total system pressure and 620 °C for 250 h. It was verified that, at constant temperature, increasing the total system pressure increases both oxygen partial pressure ($pO_2$) and carbon activity ($a_C$), simultaneously. Both samples exposed at ambient pressure showed very thin oxide scale formation and no sign of metal dusting. By contrast, samples exposed in the high-pressure experiment showed severe mass loss by metal dusting attack. Iron- and chromium-rich oxides and carbides were found as corrosion products. The distinct pressure-dependent behavior was discussed by considering both thermodynamic and kinetic aspects with respect to the protective oxide formation and pit initiation.

**Keywords** Metal dusting · Dry reforming · Syngas · Pressure

## Introduction

Metal dusting is a high-temperature corrosion phenomenon which has been a key technical obstacle in the chemical and petrochemical industries for decades. Besides its critical impact on plant safety, metal dusting can cause significant economic loss by un-predicted plant shutdowns. Since then, attempts to find protection strategies against metal dusting have been examined [1–3]. The initiation of metal dusting is referred to, among other metals, iron and nickel which are the base elements of steels and nickel alloys, respectively. Critical atmospheres for metal dusting are reducing

✉ S. Madloch
madloch@dechema.de

[1] DECHEMA-Forschungsinstitut, Theodor-Heuss-Allee 25, 60486 Frankfurt am Main, Germany

atmospheres containing supersaturated carbon ($a_C > 1$) in combination with very low oxygen partial pressures ($pO_2$). Metal dusting is expected at temperatures ranging from 450 to 900 °C, showing maximum kinetics around 625 °C [4]. The attack starts after an incubation period—provided by formation of protective oxide layers—and is followed by initiation of pits on the metal surface and propagation of the attack.

Gas composition, temperature, and pressure are the factors affecting the occurrence and initiation of metal dusting by determining the carbon activity [5]. Additionally, thermal cycling can lead to shorter incubation times by promoting oxide scale spallation [6].

The catalytically induced dissociation of carbon-containing gas species (i.e., CO, $CH_4$) by the metal surface and the subsequent formation of solid-state carbon, known as "coking," represent the initial steps of metal dusting corrosion. Three major reactions are held accountable in the literature for carbon formation:

$$\text{CO reduction reaction} : CO_{(g)} + H_{2(g)} \leftrightarrow C_{(s)} + H_2O_{(g)} \tag{1}$$

$$\text{Boudouard reaction} : 2CO_{(g)} \leftrightarrow C_{(s)} + CO_{2(g)} \tag{2}$$

$$\text{Methane cracking} : CH_{4(g)} \leftrightarrow C_{(s)} + 2H_{2(g)} \tag{3}$$

Methane cracking is thermodynamically favored at temperatures above 800 °C. The CO reduction reaction and the Boudouard reaction play an important role at lower temperatures around 600 °C where they produce very high carbon activities ($a_C$) according to Eqs. (4) and (5), respectively.

$$a_C = \exp\left(\frac{-\Delta G^0}{RT}\right) \cdot \frac{p_{H_2} p_{CO}}{p_{H_2O}} \tag{4}$$

$$a_C = \exp\left(\frac{-\Delta G^0}{RT}\right) \cdot \frac{p_{CO}^2}{p_{CO_2}} \tag{5}$$

$\Delta G^0$ represents the Gibbs free energy of the corresponding chemical reactions, $p_x$ is the partial pressure of each gaseous species, $R$ and $T$ are the gas constant and the temperature.

The increasing global demand for synthesis gas promoted the development of new processes with higher efficiencies such as the dry reforming process [7, 8]. This process involves reactions between gas components including $H_2$, CO, $CO_2$, $CH_4$, and $H_2O$ (present at a few percentages) under higher pressures than the conventional steam reforming process. According to the Le Chatelier's principle, the forward reactions of Eqs. (1) and (2) are strongly pressure dependent. The system's pressure is directly related to the partial pressures of the gas species and therefore has a strong influence on the carbon activity (Eqs. 4 and 5) [9]. The effect of the system pressure on metal dusting has been experimentally investigated by several authors [9–13]. However, the process mechanisms are still under debate. Maier et al. [10, 11] investigated the metal dusting behavior of steels containing 9–20 wt% Cr in syngas atmosphere containing 24.4% CO and 2.4% $H_2O$ at 1.9 and 5.1 bar and 560 °C. Their results showed a trend toward more severe attack by increasing

pressure. A partly better performance of ferritic steels compared to austenitic steels was explained by the higher outward diffusion coefficient of Cr in ferrite supporting the formation of a protective oxide scale. Natesan et al. [12] tested several commercial Ni-based alloys in metal dusting conditions of identical $a_C$ but different gas compositions and pressures indicating much lower incubation times of metal dusting for all tested alloys at higher system pressures.

For most high-temperature materials, the resistance to metal dusting is mainly determined by their ability to form dense and stable oxide scales at very low oxygen partial pressures. Therefore, steels and Ni-based alloys that are used for high-temperature applications contain high amounts of protective oxide-forming elements, i.e., Cr, Al, and/or Si, whose oxides, $Cr_2O_3$, $Al_2O_3$, and $SiO_2$, are all stable in typical dusting atmospheres and are non-catalytic to CO dissociation. Several authors introduced a specific term "Cr equivalent," indicating a criterion based on protective scale-forming elements for alloys "resistant" to metal dusting [14–17]. Besides Cr, Si, and Al contents were linked to the Cr equivalent. Recently, Hermse et al. [17] simply recommended the sum of Cr and Al contents to be higher than 33 for steels and Ni-based alloys to be metal dusting resistant under pressurized gas. It should be noted that Ni-based alloys show higher metal dusting resistance compared to Fe-based alloys with similar chromium contents [18]. This is correlated with the alteration of the dusting mechanism from one involving cementite formation to the one involving direct graphite precipitation. Studies on metal dusting behavior of binary Fe–Ni alloys indicated distinct increase in metal dusting resistance with increasing Ni content [13, 19]. The performance of alloy 800H in carbonaceous environments under high pressure has been studied by Nishiyama et al. [20]. It was reported that with increasing pressure, the ratio of $Cr_2O_3$ to spinel-type oxides such as $FeCr_2O_4$ decreases, leading to a more severe metal dusting attack after 100 h of exposure. To the best of the authors' knowledge, dusting of alloy 600 under pressurized gas has not been studied.

In this work, the impact of system pressure on metal dusting behavior of Fe-based alloy 800H and Ni-based alloy 600 in a CO-rich dry reforming atmosphere containing $H_2$, CO, $CO_2$, $CH_4$, and $H_2O$ was studied. The weight change behavior was investigated after exposure to CO-rich syngas at 620 °C for 250 h at 1 and 18 bar. Distinct behaviors were observed in both alloys by varying the system pressure. Microscopic and microanalytical methods were employed to reveal the corrosion and protection behavior of both alloys in atmospheres with different system pressures. The focus will be on the influence of system pressure on the potential reactions between chromium and the oxidants in the syngas atmosphere.

## Experimental Procedures

### Sample Preparation

Two commercial types of the heat-resistant austenitic alloy 800H and of the nickel-based alloy 600 were used for this study. The compositions measured by optical emission spectrometry (OES) of both alloys are given in Table 1.

The samples were cut into coupon samples of dimensions 15 × 10 × 5 mm. A drill hole was machined at the short side of each sample in order to provide hanging of the samples during the exposure tests. The sample surfaces were ground with 240- and 500-grit SiC paper, rinsed with deionized water, and degreased with acetone prior to the exposure tests.

## Exposure Tests

The exposure tests were conducted in a methane-dry-reforming atmosphere at 620 °C for 250 h. The tests were started after the experimental setups had been flushed with Ar (99.999%) for 24 h. A heating rate of 7 K/min was applied in both experiments.

The gas composition was based on the conditions in the product line of a dry reforming process. In a dry reforming process, $CH_4$ and $CO_2$ are converted to $H_2$ and CO under high pressure (15–30 bar) and high temperatures with the use of catalysts [7]. The product gas has a ratio of $H_2$:CO nearly 1 and a low amount of $CH_4$- and $CO_2$-slip originating from the feed gas as well as a few vol% of steam. The exact gas composition cannot be published due to confidential issues. Two exposure tests of the samples were carried out at identical gas composition, temperature, and exposure time but at different system pressures of 1 and 18 bar. The oxygen partial pressures and carbon activities of the two testing atmospheres at 620 °C are listed in Table 2.

The test at atmospheric pressure, MD1, was conducted in an exposure setup consisting of a gas dosage and mixture unit and a furnace. The gas flow consisting of specific amounts of $H_2$, $CO_2$, $CH_4$, and CO was regulated by mass flow controllers (*NATEC MC-100SCCM-D*) and mixed before moisturizing. The water vapor was added by conveying the gas mixture through a membrane tube (*Permapure MH 110-12F-4*) with a continuous flow of water equivalent to the required output humidity. The resulting gas mixture was carried through a three-zone tube furnace (*Carbolite TZF 12/100/900*) with a quartz tube at a flow rate of 6 l/h corresponding to a linear flow rate of 120 cm/h.

The setup that enabled metal dusting testing at high pressure, MD18, is illustrated in Fig. 1. The centerpiece of the setup is the furnace (*Carbolite HZS12/600*) with the pressure vessel, which is cast of centralloy ET 45 Micro [21]. This alloy was selected due to its outstanding corrosion resistance owing to its high chromium content (35 wt%) and the mechanical stability at high temperatures and pressures.

**Table 1** Composition of alloys studied in this work

| | Elements (wt%) | | | | | | | | | | |
|---|---|---|---|---|---|---|---|---|---|---|---|
| Material | Fe | Ni | Cr | C | Si | Al | Ti | Mn | Cu | S | P |
| Alloy 800H | Bal. | 30.72 | 20.24 | 0.058 | 0.351 | 0.404 | 0.323 | 0.734 | 0.089 | 0.0008 | 0.019 |
| Alloy 600 | 8.31 | Bal. | 17.08 | 0.033 | 0.337 | 0.158 | 0.214 | 0.262 | 0.068 | 0.0054 | <0.001 |

**Table 2** Total system pressure, oxygen partial pressure, and carbon activity of the test conditions at 620 °C

| | $p$ (bar) | $pO_2$ (atm) | $a_C$ |
|---|---|---|---|
| MD1 | 1 | $1.2 \times 10^{-24}$ | 9 |
| MD18 | 18 | $2.8 \times 10^{-23}$ | 163 |

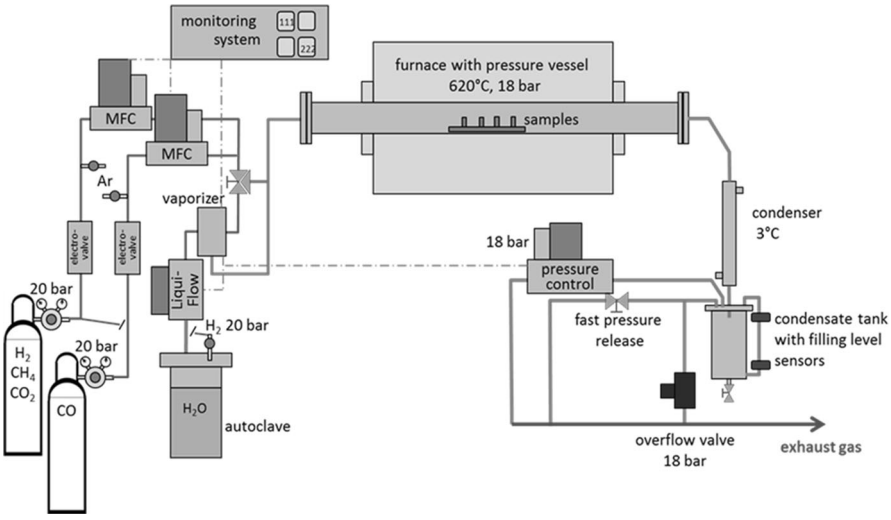


**Fig. 1** Schematic illustration of the MD18 exposure setup

Mass flow controllers (*Bronkhorst EL-FLOW® Select*) were used to regulate the flow rates of the gas at the similar rate used under atmospheric pressure test (6 l/h). The steam was generated by a combined system of an autoclave (*Parr model 4913*), a water dosage unit (*Bronkhorst LIQUI-FLOW® μ-flow*), and a vaporizer (*Bronkhorst W-101A Evaporator*). A pressure of 20 bar was applied on water in the autoclave in order to transport it through the dosage unit. Very small dosage of water into the vaporizer and subsequent evaporation of the water into the flowing gas provided the required moisture in the process.

When the gas composition had been adjusted, the system was pressurized to 18 bar by a pressure control unit (*Bronkhorst FLOW-BUS®*). After the gas had passed the sample chamber, the water vapor was condensed in a cooling unit and the condensed water was collected in a condensate tank (*Parr custom-made product*).

After isothermal exposure, specimens were cooled in the furnace under Ar atmosphere without applying a cooling rate.

The exposed specimens were cleaned in ethanol with the use of an ultrasonic bath in order to remove the loose coke. Net mass changes were obtained by weighing the dried samples.

### Analytical Examination

Sample surfaces were analyzed by SEM (*Philips XL40*). Microscopic and chemical analysis was conducted on cross sections of the samples using light optical microscopy (LOM; *Leica DLMA*) and electron probe microanalysis (EPMA, *Jeol JXA-8100*). The EPMA had a spatial resolution of ca. 1 μm.

### Thermodynamic Calculations

Thermodynamic parameters such as Gibbs free energy ($\Delta G$) of reaction equations were determined using the thermodynamic calculation software *FactSage*$^{TM}$*6.1*.

## Results

### Gravimetric Analysis

Even the first visual inspection of the tested samples revealed a significant impact of the system pressure on the metal dusting behavior of the studied alloys. Although both testing conditions provided the required condition (see Table 2) to promote metal dusting corrosion, only alloys exposed to the 18-bar atmosphere suffered from metal dusting after 250 h. They showed massive coke formation and numerous metal dusting pits of different sizes on the surface. In contrast, the samples exposed to the testing conditions at 1 bar system pressure did not show any sign of coking or metal dusting. Their surfaces exhibit tempering colors indicating formation of a thin oxide layer.

The weight change results of the samples exposed to the metal dusting conditions at 1 and 18 bar are plotted in Fig. 2. At 1 bar, both alloy 800H and alloy 600 show very low mass gains of 0.04 and 0.03 mg/cm$^2$, respectively. In contrast, at 18 bar, alloy 800H sample and alloy 600 showed significant mass losses of $-102.00$ and $-20.70$ mg/cm$^2$, respectively. However, it should be noted that the extent of mass loss in alloy 600 was markedly below that of alloy 800H (80% lower).

### Surface Analysis

Secondary electron (SE) images of the surfaces of the post-exposure specimens are shown in Fig. 3. It is evident that both alloy 600 and alloy 800H exhibit continuous and thin surface oxide layers after exposure at 1 bar (see Fig. 3a, b). It should be noted that the parallel lines across the surface represent scratches on the metal surface which were present prior to exposure and are covered with a thin oxide layer.

The samples exposed at 18 bar system pressure are covered with numerous circular metal dusting pits that are coalescing at several points. It should be noted that the average size of pits is significantly larger on alloy 800H than that on alloy 600 (see Fig. 3c, d and note the difference in scale bars). The larger pits on the alloy 800H sample correspond to the high weight loss compared to alloy 600 showing

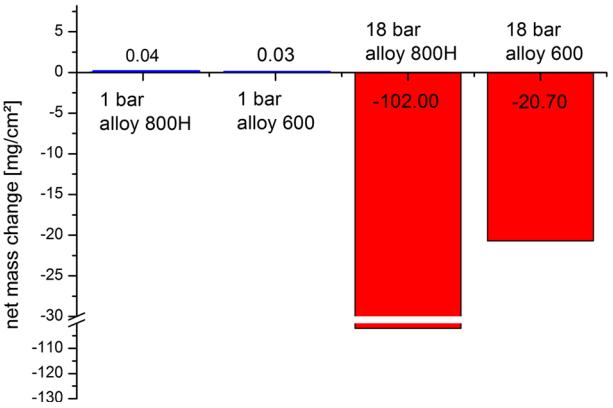


**Fig. 2** Net mass changes of the alloys after exposure under metal dusting atmosphere at 620 °C for 250 h as a function of total system pressure

smaller pits. Figure 3e, f shows the surface morphology of the borders between the intact oxide surface and a pit at higher magnification. Unlike the structure at the intact metal surface oxide, large grain and non-compact oxides are evident leading to a rather rough surface.

## Cross-sectional Analysis

Cross-sectional BSE images and element distribution maps of alloy 800H and alloy 600 samples after exposure in metal dusting environment at 1 bar are shown in Fig. 4. Additionally, concentration profiles of the main elements (C, O, Fe, Cr, Ni) are shown in Fig. 5a, b.

Both alloys show continuous but very thin ($\approx$1–1.5 µm) oxide layers. The low thickness of the oxide layers was expected, considering the moderate test temperature (620 °C) and exposure time (250 h). Since the thicknesses of the oxide scales are at the border of the spatial resolution of the EPMA, their compositions can hardly be determined.

Thermodynamic calculations revealed that chromium oxide is the most stable oxide in both alloys at the extremely low oxygen partial pressure of $1.2 \times 10^{-24}$ atm and 620 °C. Considering thermodynamic stability of potential oxides in tested atmosphere and the relatively low testing temperature, the thin Cr-rich layer between the electroplated Ni and the substrate is most likely chromium oxide. In accordance with the thin scale, no significant Cr depletion was detected at the subscale substrate (see Figs. 4 and 5).

Underneath the oxide scales, enrichments of carbon of 4.5 at% in alloy 800H and of 2.7 at% in alloy 600 were detected. The thin carbon-enriched layer can be formed during the buildup of the continuous chromium oxide which afterward protects the substrate from the inward carbon diffusion.

The optical micrograph of a metal dusting pit formed on alloy 800H after exposure at 620 °C and 18 bar is shown in Fig. 6a. The pit has a depth of

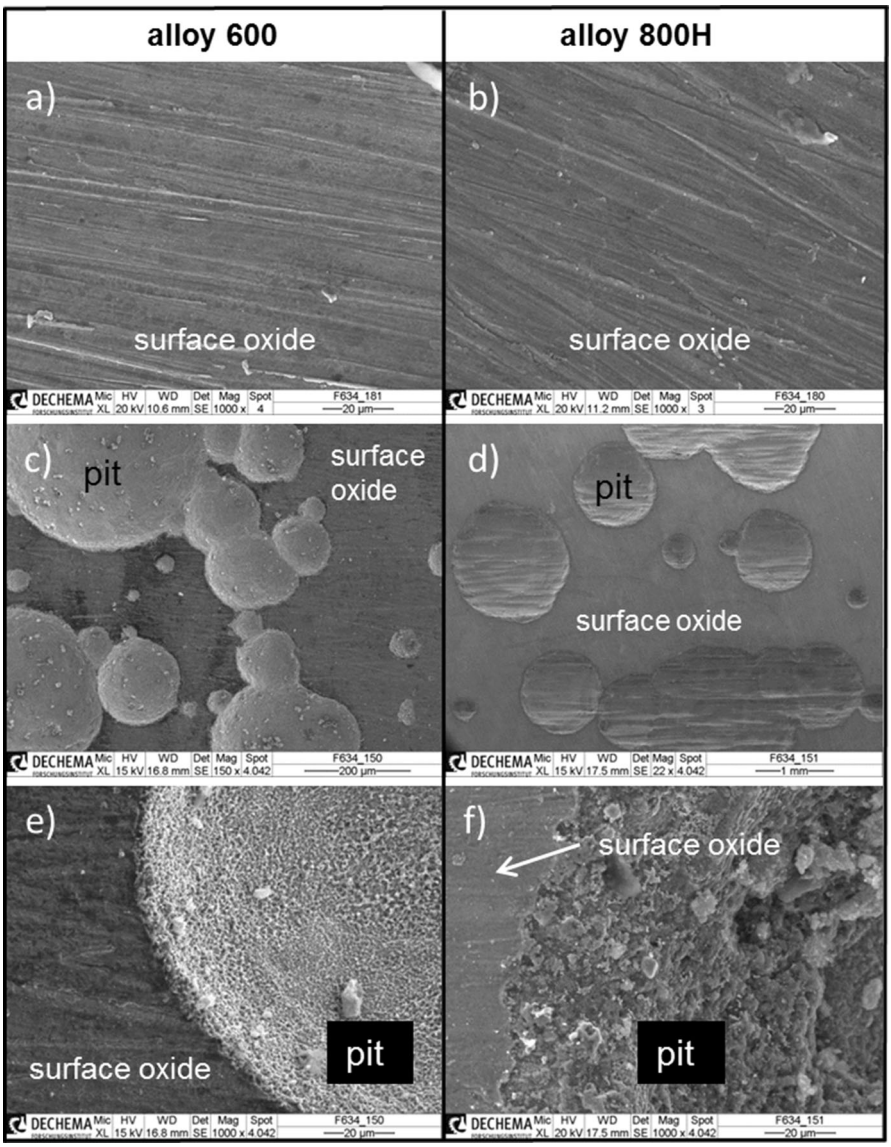


**Fig. 3** SE images of sample surfaces of alloy 600 (**a**) and alloy 800H (**b**) after exposure at 1 bar. Sample surfaces covered with metal dusting pits after exposure at 18 bar and transition of oxide/pit (alloy 600 (**c**, **e**); alloy 800H (**d**, **f**)). Note the scale bar and the size of pits in (**c**) and (**d**)

100–110 µm from the surface and is approximately 300 µm in diameter. Its shape indicates a coalescence of originally two smaller pits during the exposure. Element concentration profiles through the middle of the pit as well as at the non-attacked surface are illustrated in Fig. 7. Significant carbon enrichment underneath the pit surface was detected, implying that the substrate below the pit was strongly

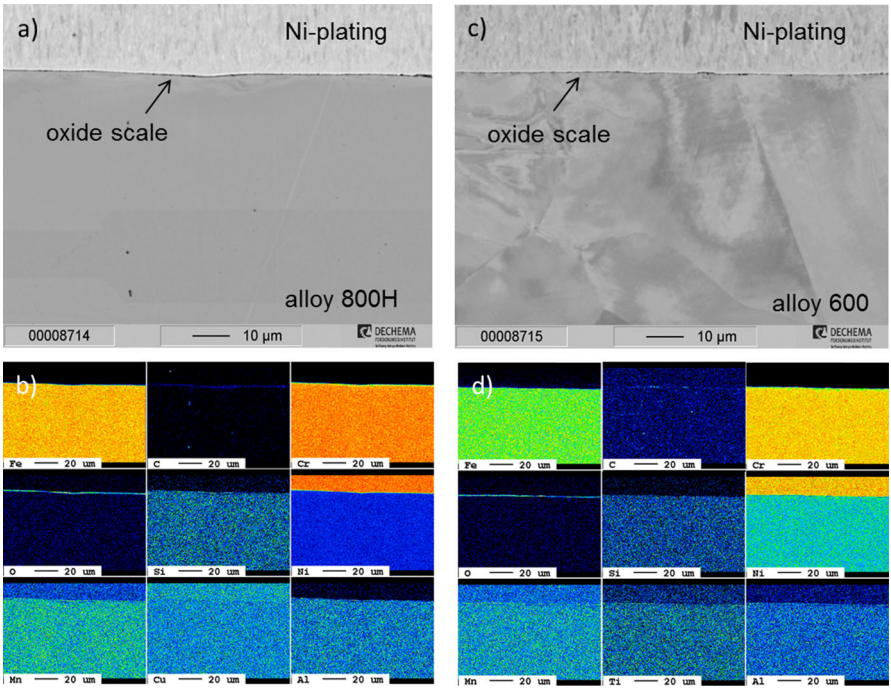


**Fig. 4** BSE images and element distribution maps of alloy 800H (**a**, **b**) and alloy 600 (**c**, **d**) samples after exposure at 1 bar and 620 °C under metal dusting atmosphere

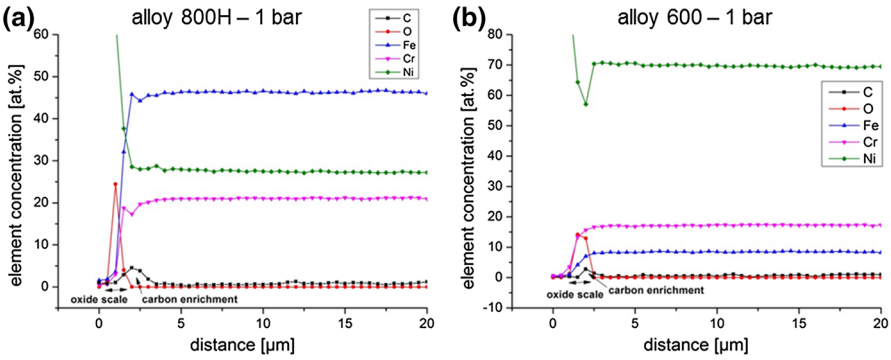


**Fig. 5** Quantitative line scan of alloy 800H (**a**) and 600 (**b**) samples exposed at 1 bar and 620 °C under metal dusting atmosphere

carburized. Figure 6b shows a higher magnification of the pit shown in Fig. 6a. The corresponding element distribution maps are shown in Fig. 6c.

The comparison between the non-attacked neighboring surface and the pit surface indicates that the pit shows a rough surface covered with a thick oxide, while the non-attacked region shows an even surface covered with a thin oxide. Element distribution maps demonstrate that the oxide formed on the pit surface is

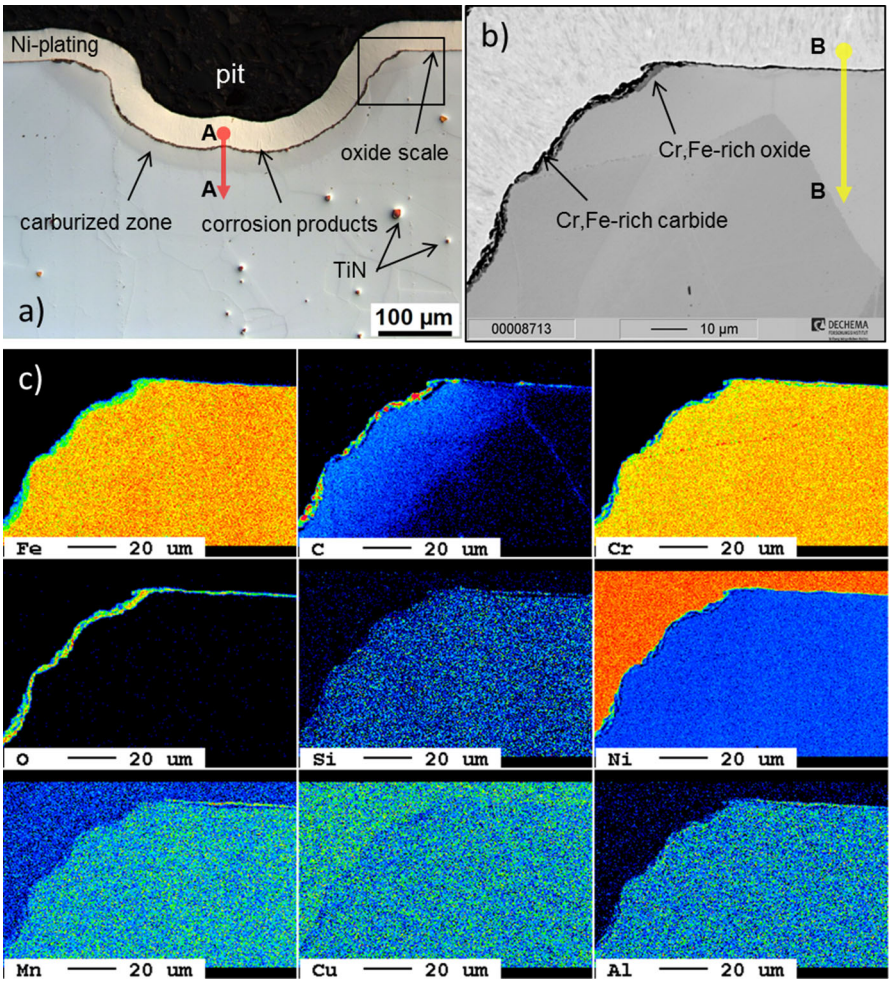


**Fig. 6** Cross-sectional image of a metal dusting pit (**a**) of alloy 800H after exposure at 18 bar and 620 °C under metal dusting atmosphere. The *inset* in (**a**) is shown at higher magnification in (**b**) as well as the element distribution maps (**c**)

non-continuous and is composed of Fe-rich oxides and embedded carbide particles. Because the carbides are too small for detecting their composition via EPMA, future TEM investigation is planned in order to determine the type of carbides. The oxide formed on the non-attacked surface consists of continuous chromium oxide. Besides, the composition of the subsurface region resembles the protectiveness of the oxide scales formed on the corresponding surfaces. The significant depth of carbon enrichment (ca. 40 µm) in the pit's subsurface area is evident while hardly any can be seen in the subsurface zone of the pit-free area.

The BSE micrograph and the corresponding element distribution maps of a representative pit formed on alloy 600 after 250 h exposure at 18 bar and 620 °C are shown in Fig. 8. The comparison between the geometry and the size (10 µm) of

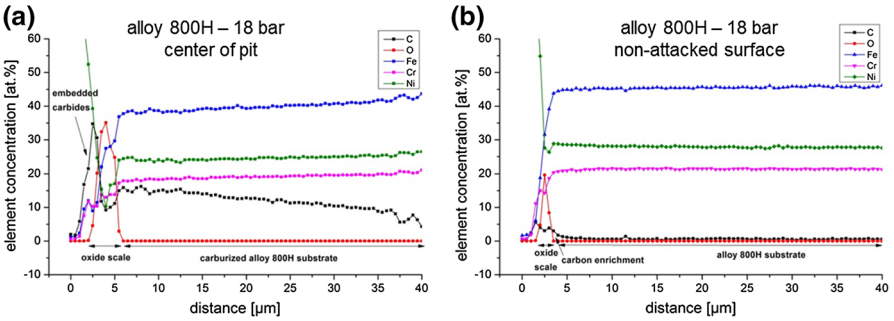


**Fig. 7** Quantitative line scan of alloy 800H exposed under metal dusting atmosphere at 18 bar and 620 °C. The position of each line scan is marked with A–A (**a**) and B–B (**b**) in Fig. 6

the pit formed on alloy 600 (Fig. 8) and those shown previously on alloy 800H under similar conditions (Fig. 6) indicates that the pit formed on alloy 600 is in the initial stage. The quantitative concentration profile through the middle of the pit (C–C) reveals the composition of the oxidation products and the phases in the pit and at the subsurface area, respectively (Fig. 8c).

At the unaffected surface, a scale consisting of (Mn, Cr, Fe)-rich oxide, supposedly in the form of $(Cr, Mn)_2O_3$, or $(Mn,Fe)Cr_2O_4$ formed. In addition, strong oxide formers such as Si, Ti, Al are enriched, but due to their low concentration in alloy 600 their oxides are discontinuous (see Si, Ti, and Al maps in Fig. 8b). In the pit, chromium- and iron-rich carbides as well as the oxides which were also found at the unaffected surface were identified. Below the pit, a circular zone has been affected by carburization. Figure 8d illustrates the different phases formed within and around the pit, schematically.

## Discussion

The results showed that both alloys are in the incubation stage after exposure at ambient pressure for 250 h. After identical exposure at 18 bar, both alloys showed metal dusting propagation after 250 h with the attack being more severe on alloy 800H than on alloy 600. This underlines the marked impact of pressure as alloys were both exposed to the metal dusting promoting condition. Generally, one can understand the process as a competition between the formation of thermodynamically stable oxides and carbon formation and diffusion into the metal substrate. Thermodynamic parameters such as carbon activity and oxygen partial pressure can greatly influence either side of this competition and therefore need to be considered. Since parameters such as syngas composition and temperature were kept constant for both exposure tests in this work, system pressure is the only thermodynamic variable affecting both carbon activity and oxygen partial pressure. According to thermodynamic calculations, increasing the system total pressure significantly increases the carbon activity by a factor of 18, while the $pO_2$ was increased by one order of magnitude (see Table 2). Since both low-pressure and high-pressure

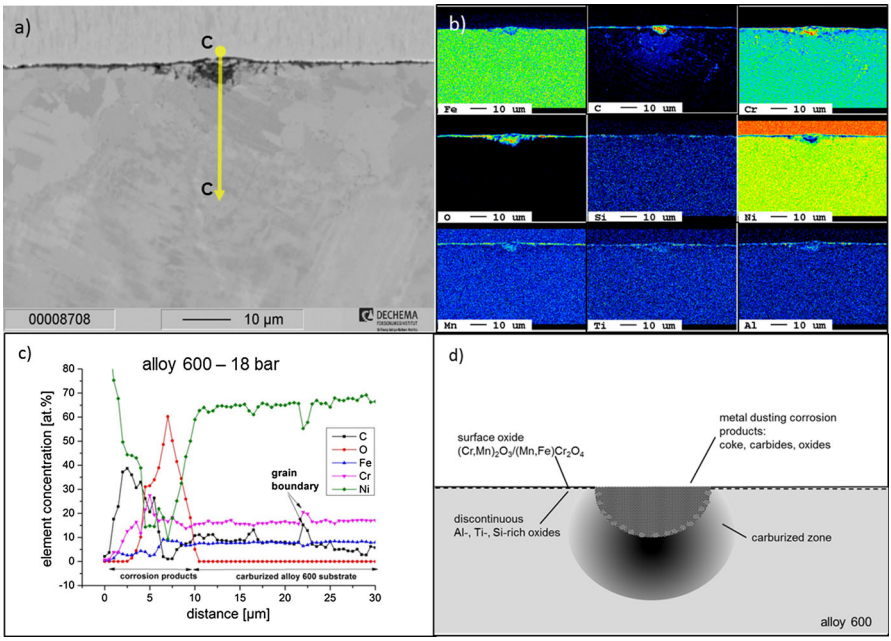


**Fig. 8** **a** Cross-sectional BSE image, **b** EPMA element distribution maps, and **c** a selected line scan (C–C) of alloy 600 after exposure under metal dusting atmosphere at 620 °C and 18 bar. The metal dusting pit is filled with corrosion products. **d** Schematic illustration of the metal dusting pit and the surrounding surface area

experiments provided high carbon activities ($a_C > 1$) required for metal dusting attack, the distinct protection behavior of alloys at ambient and high pressures is somewhat surprising. Under ambient total system pressure, both alloys could form well-established protective chromium oxide on the metal surface while the formation of such oxides was hindered under high total system pressures leading to the formation of faster growing oxides such as $MnCr_2O_4$/$FeCr_2O_4$. The higher growth rate of these oxides can lead to the formation of growth stress-induced defects which in turn can deteriorate the protective behavior. Similar behavior was observed under normal pressure and high-pressure metal dusting conditions [9, 20]. Thus, the total system pressure can affect the ability to form a protective oxide. Comparing the Cr concentration profiles of all investigated samples (Figs. 5, 7, 8c), only a negligible Cr depletion was observed underneath the oxide scales. The subscale chromium content remained at about 21.1 and 17.3 at% in alloys 800H and 600, respectively, which did not show a marked deviation from the initial chromium content of the alloys. This is somewhat expected considering the thin chromium-rich oxide layer formation and rather low temperature for Cr diffusion in austenite. Nevertheless, considering the spatial resolution of the EPMA technique (ca. 1 µm), possible Cr depletion at this range of distance from the surface cannot be resolved and would require high-resolution techniques.

Considering that the oxygen partial pressure in the studied atmospheres $pO_2(gas)$ is higher than the equilibrium partial pressure for $Cr_2O_3$ formation $pO_2(Cr_2O_{3(eq)})$ at 620 °C at both pressures, formation of chromium oxide is thermodynamically favored. In the process, $H_2O$, $CO_2$, and CO are the possible oxidants of chromium, according to Eqs. (6)–(9).Oxidation by carbon dioxide or water vapor:

$$2Cr_{(s)} + 3CO_{2(g)} \rightarrow Cr_2O_{3(s)} + 3CO_{(s)} \tag{6}$$

$$2Cr_{(s)} + 3H_2O_{(g)} \rightarrow Cr_2O_{3(s)} + 3H_{2(g)} \tag{7}$$

Oxidation and carburization by CO:

$$2Cr_{(s)} + 3CO_{(g)} \rightarrow Cr_2O_{3(s)} + 3C_{(s)} \tag{8}$$

And the inverse microclimate reaction [22, 23]:

$$\frac{27}{2}Cr_{(s)} + 3CO_{(g)} \rightarrow Cr_2O_{3(s)} + \frac{1}{2}Cr_{23}C_{6(s)} \tag{9}$$

The Gibbs free energies calculated for these reactions at total system pressures of 1 bar and 18 bar at a temperature of 620 °C are shown in Table 3. The actual partial pressures of each gas component (inlet pressure) were taken into account for the calculations.

All reactions show a negative Gibbs free energy. From a thermodynamic point of view, oxidation of Cr by CO provides the highest energy release (Eqs. 8 and 9). These reactions on the one hand strongly compete with the catalytic metal dusting reactions (Eqs. 1 and 2), which result in carbon formation. On the other hand, oxidation of Cr by CO competes with oxidation of Cr by $CO_2$ and $H_2O$ during oxide formation. Especially in the initial stage of oxidation, formation and diffusion of carbon into the alloy substrate occur before a continuous protective layer is formed. This hypothesis can be supported by the thin carbon-enriched layers that were found right below the oxide scale (Fig. 5). As soon as a continuous oxide film is formed at the surface, it reduces further catalytic carbon formation (coking) and ingress.

In highly alloyed materials that form protective oxide scales under metal dusting conditions, metal dusting is believed to be initiated by local defects in the oxide scale. These defects can be induced by accumulated growth stresses in the oxide

**Table 3** Gibbs free energy of Eqs. (6)–(9) at 620 °C and 1 bar as well as 18 bar

| | $\Delta G^{1bar}_{620°C}$ (kJ/mol) | $\Delta G^{18bar}_{620°C}$ (kJ/mol) |
|---|---|---|
| $2Cr_{(s)} + 3CO_{2(g)} \rightarrow Cr_2O_{3(s)} + 3CO_{(g)}$ | −278.8 | −278.8 |
| $2Cr_{(s)} + 3H_2O_{(g)} \rightarrow Cr_2O_{3(s)} + 3H_{2(g)}$ | −292.5 | −292.5 |
| $2Cr_{(s)} + 3CO_{(g)} \rightarrow Cr_2O_{3(s)} + 3C_{(s)}$ | −328.8 | −393.3 |
| $\frac{27}{2}Cr_{(s)} + 3CO_{(g)} \rightarrow Cr_2O_{3(s)} + \frac{1}{2}Cr_{23}C_{6(s)}$ | −519.4 | −583.8 |

scale leading to crack formation [24–27] or by precipitations such as carbides or nitrides (e.g., TiN precipitations in alloy 800H, see Fig. 6a) when located at the oxide–metal interface disturbing the formation of a continuous oxide layer.

In order to protect the substrate against metal dusting, such oxide defects should be healed by fresh oxide formation to keep the substrate separated from the corrosive atmosphere. Considering the chromium concentration behavior during oxidation, it is well known that in case that the primary oxide layer is damaged, enough chromium reservoir would be required to heal the damaged scale [28]. Considering the observed low Cr depletion, it can be excluded that the metal dusting pit initiation occurred due to a strong Cr depletion preventing the healing of the damaged oxide scale.

Oxidation of Cr by $H_2O$ and $CO_2$ consumes and releases the same amount of gas molecules and consequently is not pressure dependent (Le Chatelier's principle). This is the reason for the same values of the Gibbs free energy for the reactions at 1 bar and 18 bar (Table 3). In contrast, Eqs. (8) and (9) are strongly pressure dependent. Their forward reactions are favored at higher pressures, resulting in a higher Gibbs free energy at higher pressures (Table 3).

Besides thermodynamic considerations, the effect of pressure on kinetic parameters such as surface coverage of the adsorbed gas species should be considered when studying surface–gas reactions. Assuming the Langmuir adsorption isotherm, the degree of surface coverage ($\Theta$) increases with increasing pressure ($p$) according to the following equation [29]:

$$\theta = \frac{K \cdot p}{1 + K \cdot p} \tag{10}$$

$K$ is the equilibrium constant, which is further determined by the ratio of adsorption constant $k_{ad}$ to desorption constant $k_{des}$. At high pressure, the degree of surface coverage approximates to 1. This formula is valid under the assumption that no interaction between gas molecules takes place and all adsorption sites are equivalent. Increasing the total pressure, therefore, does not affect the fractional coverage of each individual species. However, it is expected that different gas species show different adsorption behavior. Recently, Kahle conducted an extensive study on the reaction kinetics of oxidation and reforming of $H_2$, CO, and $CH_4$ over platinum catalysts [30]. She developed a simulation-based model for elementary reactions at 20 bar at varying temperatures and gas compositions (including $H_2$,CO, $CO_2$, $CH_4$, and $H_2O$) which was validated by experiments. The adsorption energy of $H_2$ and $CO_2$ was shown to be significantly lower than that of CO on (Pt) surfaces. Therefore, they easily desorbed from the surface. The remaining $CO_2$ reacted with the adsorbed H(Pt) to form CO(Pt) and hydroxyl groups (OH(Pt)). On the other hand, $H_2O$ adsorbed at low temperature started to desorb at $T \approx 600$ K (327 °C) ending at about $\approx$1000 K (727 °C). Simultaneously, CO started adsorbing at $\approx$600 K, reaching its maximum partial coverage at 850 K (close to the testing temperature of this work). CO showed a dominant coverage among the gas species used. The above-mentioned findings were stated for Pt catalysts. It is known that iron and nickel also show catalytic activity with regard to metal dusting [3].

Considering the comparable atmosphere used in this study and that of Kahle, it is suggested that CO adsorption on the exposed surfaces dominates with increasing pressure. This means, when the oxide scale formed in the testing atmosphere failed locally, local metallic surface was exposed to the atmosphere in which CO preferentially adsorbs. This led to the initiation of the metal dusting process following reactions (8) and (9) as explained above. It is noteworthy that Hermse reported stronger metal dusting attack with an increase in pCO [31]. This, in addition to the preferred adsorption behavior of CO on metallic surfaces, can intensify the extent of metal dusting attack.

Besides the degree of coverage, also the collision frequency of the gas molecules to the metal surface increases with pressure. This increase can be expected to be more dominant for CO species as the dominant constituent in the syngas atmosphere. Thus, a faster reaction kinetic can be expected for reactions (8) and (9).

Concluding the thermodynamic and kinetic considerations, Cr oxidation by CO becomes more important at higher pressures and is accompanied by the formation of carbon and/or carbides. When taking place at the metal surface below an oxide scale defect, these reactions lead to a very strong local Cr consumption and Fe–Ni enrichment. Thus, such spots are prone to metal dusting initiation. It should be noted that these spots cannot be characterized by post-exposure metallographic techniques since the microanalytical investigations were done after the metal dusting attack had proceeded. The presented aspects may explain why much higher amounts of Cr are required for a given alloy for protection under high-pressure metal dusting conditions than under atmospheric pressure or oxidation in air.

## Conclusions

The present study showed that the total system pressure strongly affects the performance of alloys in metal dusting atmospheres. Exposing alloys prone to metal dusting led to many different reactions that simultaneously took place at the metal surface. Oxide formation was evident at ambient and at 18 bar pressure. At higher pressures, other reactions such as oxidation by CO became more important. Comparison with the literature suggests that the evaluation of the adsorption behavior of the gas species in the testing atmosphere shows a preferred CO adsorption over other species. In the case of local oxide failure, oxidation of Cr by the adsorbed CO resulted in carbon or carbide formation leading to high local chromium consumption. These reactions are followed by the metal dusting reactions on Fe- and Ni-rich surfaces. As a consequence, the initiation of a metal dusting pit (incubation time) was shifted toward shorter times with increasing total system pressure.

**Acknowledgements** We gratefully thank the German Federal Ministry for Economic Affairs and Energy for the financial support. This research was done within the scope of the project “DRYREF2.”

## References


1. P. A. Lefrancois, and W. B. Hoyt, *Corrosion* **19**, 360 (1963).
2. R. F. Hochman, in Proceedings of the 4th International Congress on Metal Corrosion, NACE, ed. N. E. Hammer, (NACE, 1972), p. 258.
3. D. J. Young, J. Zhang, C. Geers, and M. Schütze, *Materials and Corrosion* **62**, 7 (2011).
4. R. Schneider, E. Pippel, J. Woltersdorf, S. Strauß, and H. J. Grabke, *Steel Research* **68**, 326 (1997).
5. D. J. Young, and J. Zhang, *Journal of the Minerals, Metals and Materials Society* **64**, 1461 (2012).
6. Y. Nishiyama, N. Otsuka, and T. Kudo, *Corrosion Science* **48**, 2064 (2006).
7. E. Schwab, A. Milanov, S. A. Schunk, A. Behrens, and N. Schoedel, *Chemie Ingenieur Technik* **87**, 347 (2015).
8. M. Peters, B. Köhler, W. Kuckshinrichs, W. Leitner, P. Markewitz, and T. E. Müller, *ChemSusChem* **4**, 1216 (2011).
9. K. Natesan, and Z. Zeng, 14 Feb., 2007, 2005.
10. M. Maier, J. F. Norton, and P. D. Frampton, *Materials and Corrosion* **49**, 330 (1998).
11. M. Maier, J. F. Norton, and P. Puschek, *Materials at High Temperatures* **17**, 347 (2000).
12. K. Natesan, and Z. Zeng, *Development of Materials Resistant to Metal Dusting Degradation*, (U.S. Department of Energy, 2006).
13. A. Rouaix-Vande Put, K. A. Unocic, M. P. Brady, and B. A. Pint, *Corrosion Science* **92**, 58 (2015).
14. C. M. Schillmoller, *Chemical Engineering* **93**, 83 (1986).
15. S. B. Parks, and C. M. Schillmoller, *Hydrocarbon Processing* 53 (1996).
16. D. Röhnert, M. Schütze, and T. Weber, 27 Mar., 2007, NACE, Nashville, 2007.
17. C. G. M. Hermse, and H. van Wortel, EUROCORR 2008, Edinburgh, 2008.
18. E. Pippel, J. Woltersdorf, and H. J. Grabke, in *Corrosion by carbon and nitrogen: Metal dusting, carburisation and nitridation (EFC 41)*, eds. by H. J. Grabke and M. Schütze (Woodhead Publishing, Cambridge, 2007), p. 49.
19. J. Zhang, and D. J. Young, *Oxidation of Metals* **70**, 189 (2008).
20. Y. Nishiyama, K. Kitamura, and N. Otsuka, *Materials Science Forum* **595–598**, 649 (2008).
21. Schmidt + Clemens GmbH & Co.KG, Centralloy® ET 45 Micro Material Data Sheet, 2009.
22. H.-J. Christ, U. Künecke, K. Meyer, and H. G. Sockel, *Oxidation of Metals* **30**, 27 (1988).
23. D. Kumar, R. R. Adharapurapu, T. M. Pollock, and G. S. Was, *Metallurgical and Materials Transactions A* **42A**, 1245 (2011).
24. H. J. Grabke, K. Ohla, J. Peters, and I. Wolf, *Materials and Corrosion* **34**, 495 (1983).
25. A. Soleimani-Dorcheh, *Oxidation-Nitridation of Chromium at High Temperatures and its Mitigation by Alloying* (Doctoral Thesis, RWTH Aachen, Shaker Verlag, Herzogenrath, 2017).
26. P. Kofstad, *Oxidation of Metals* **24**, 265 (1985).
27. P. Kofstad, *Oxidation of Metals* **44**, 3 (1995).
28. D. P. Whittle, G. C. Wood, D. J. Evans, and D. B. Scully, *Acta Metallurgica* **15**, 1747 (1967).
29. J. Hagen, *Technische Katalyse - Eine Einführung*, (Wiley-VCH, Weinheim, 1996).
30. L. C. S. Kahle, Institute for Chemical Technology and Polymer Chemistry, Karlsruhe Institute of Technology, 2013.
31. C. G. M. Hermse, NACE International, 2011.